

Cluster-diagrammatic D-TRILEX approach to non-local electronic correlations

Félix Fossati¹ and Evgeny A. Stepanov^{1,2}

¹*CPHT, CNRS, École polytechnique, Institut Polytechnique de Paris, 91120 Palaiseau, France*

²*Collège de France, Université PSL, 11 place Marcelin Berthelot, 75005 Paris, France*

In this work, we extend the theoretical approach known as “D-TRILEX”, developed for solving correlated electronic systems, to a cluster reference system for the diagrammatic expansion. This framework allows us to consistently combine the exact treatment of short-range correlation effects within the cluster, with an efficient diagrammatic description of the long-range charge and spin collective fluctuations beyond the cluster. We demonstrate the effectiveness of our approach by applying it to the one-dimensional nano-ring Hubbard model, where the low dimensionality enhances non-local correlations. Our results show that the cluster extension of D-TRILEX accurately reproduces the electronic self-energy at momenta corresponding to the Fermi energy, in good agreement with the numerically exact quantum Monte Carlo solution of the problem, and outperforms significantly more computationally demanding approach based on the parquet approximation. We show that the D-TRILEX diagrammatic extension drastically reduces the periodization ambiguity of cluster quantities when mapping back to the original lattice, compared to cluster dynamical mean-field theory (CDMFT). Furthermore, we identify the CDMFT impurity problem as the main source of the translational-symmetry breaking and propose the computational scheme for improving the starting point for the cluster-diagrammatic expansion.

I. INTRODUCTION

The theoretical description of strongly correlated materials relies on solving interacting electronic model Hamiltonians. Accounting for the electron-electron interaction can significantly modify the characteristics of a non-interacting system. In the weak-coupling regime, these interactions renormalize single-particle properties such as the effective electron mass and the spectral function. This behavior is well described by Landau Fermi liquid theory [1, 2], and perturbative diagrammatic methods such as the *GW* [3–5] or the fluctuation-exchange (FLEX) [6–8] approximations yield reasonable results. However, these methods break down as the interaction strength increases. In the strong-coupling regime, non-perturbative approaches such as dynamical mean-field theory (DMFT) [9] are required to capture emergent strongly correlated phenomena, including the Mott metal-insulator transition [10, 11] and Hund’s metal behavior [12, 13], which lie beyond a weak-coupling-like theoretical description.

The single-site DMFT formulation assumes a purely local self-energy and thus neglects spatial electronic correlations. This approximation, while exact in the limit of infinite dimensions [14, 15], leads to a number of limitations in realistic low-dimensional systems. For instance, DMFT cannot capture the momentum-dependent renormalization of the electronic spectral function induced, for example, by strong magnetic fluctuations. In particular, such fluctuations may lead to a momentum-dependent suppression of the density of states at the Fermi surface, known as the nodal-antinodal dichotomy (see, e.g., Ref. [16]). In addition, DMFT is not designed to describe small-scale systems, such as dimer or one-dimensional models, where accounting for inter-site correlations is essential (see, e.g., Refs. [17, 18]).

Cluster dynamical mean-field theory (CDMFT) [19–25] is the most natural non-perturbative extension that incorporates non-local correlations beyond the single-site DMFT. By embedding a finite cluster into a self-consistent bath, CDMFT explicitly accounts for short-range correlations within the cluster, which are treated numerically exactly. This construction

captures singlet formation and local-moment physics, thereby accounting for the effects that are believed to be responsible for strong-coupling antiferromagnetism, pseudogap formation, and high-temperature superconductivity [20, 26–33].

Despite many successes, CDMFT has several conceptual and practical difficulties. First, the Hilbert space of the impurity problem, that has to be solved at every iteration in the DMFT self-consistent loop, grows exponentially with the number of cluster sites N_c , so the computational cost scales as d^{N_c} , where d is the number of degree of freedom for one site. Quantum Monte Carlo (QMC) [34] and continuous-time quantum Monte Carlo (CT-QMC) methods [35–41] eliminate the need for exact diagonalization and allow one to avoid the exponential scaling with N_c . However, QMC and CT-QMC approaches are affected by the infamous fermionic sign problem [42–44], which worsens with the number of lattice sites and is particularly severe for hybridization-expansion (CT-HYB) based methods [39, 41, 45]. Second, CDMFT breaks the translational symmetry of the original lattice, as it treats bonds within and between clusters in fundamentally different ways: the intra-cluster bonds are handled non-perturbatively within the exactly solved impurity problem, while the inter-cluster bonds are effectively treated as non-interacting. Reinstating translational symmetry requires a periodization step, in which the cluster outputs are re-expressed as lattice quantities under the assumption of the original lattice symmetry. The outcome of this procedure depends sensitively on which quantity is periodized – Green’s function, self-energy, or cumulant – and can lead to noticeably different single-particle spectra and even changes in the inferred Fermi surface (FS) topology [46, 47]. Third, CDMFT calculations cannot provide a good resolution in momentum space and thus are unable to resolve fine momentum-space structures, such as small Fermi pockets, shadow bands, momentum-dependent pseudogaps, or sharp dispersions of collective modes [16, 46–48], without moving to much larger (and hence computationally prohibitive) clusters. Finally, CDMFT neglects correlations that extend beyond the cluster. As a result, CDMFT with relatively small clusters tends to overestimate the critical tem-

peratures for magnetic transitions [20, 26, 49], underestimate the critical interaction strength for the Mott transition [25], and cannot capture the momentum-resolved spectral functions of long-range collective electronic fluctuations such as plasmons and magnons.

Alternatively, non-local correlations beyond the single-site DMFT can be introduced diagrammatically [50, 51]. In rare cases, the diagrammatic extensions of DMFT enable resummation of all Feynman diagrams up to a given order [52–54] using the diagrammatic Monte Carlo technique [55, 56]. However, in most cases, this procedure is computationally expensive, and the diagrammatic expansion is typically restricted to a subset of leading contributions, as in the *GW* extension of DMFT [57–63], the two-particle self-consistent (TPSC) extension of DMFT [64–68], the dual fermion (DF) [69–72], the dual boson (DB) [73–78], the dynamical vertex approximation (D Γ A) [49, 79–82], the triply irreducible local expansion (TRILEX) [83–85], and the dual TRILEX (D-TRILEX) [17, 86, 87] methods. The diagrammatic approaches have produced a series of notable successes, precisely because they self-consistently augment the local physics with spatial correlations at all length scales, including the genuinely long-range fluctuations that remain out of reach for cluster approaches. As the result, the diagrammatic methods enable accurate description of the Néel transition [71, 88–91], especially in the regime where the magnetic fluctuations have very large correlation length [92–95]. The diagrammatic extensions of DMFT are also successful in addressing the superconducting state [33, 85, 96–99], even when compared with the already reliable results obtained from cluster methods [20, 100, 101]. This improvement is often traced back to the ability of the diagrammatic methods to account for the long-range strong spin fluctuations [33, 90, 93]. Furthermore, the diagrammatic extensions of DMFT are also capable of addressing the charge-ordered state [60, 74–76, 102–104] and describing momentum-resolved spectral functions for collective charge [59, 105, 106] and spin [77, 83, 107–109] fluctuations. These methods, however, remain perturbative beyond the local level, so their accuracy strongly depends on the subset of diagrams and varies between different physical regimes. It is still possible to go beyond these approximations using more sophisticated diagrammatic techniques. However, the downside is that the resulting diagrammatic structure become too complex to be applied efficiently to multi-orbital systems.

Below, we turn to the D-TRILEX scheme [86], which offers a good compromise between accuracy and cost of numerical calculations [17, 87]. D-TRILEX simultaneously treats collective electronic fluctuations in the charge and spin channels on equal footing without the Fierz-ambiguity problem. The single-particle and collective fluctuations are treated self-consistently within the functional formulation of the method [17], so that non-local electronic correlations are coherently incorporated beyond DMFT [16, 33, 103, 110–112]. The D-TRILEX approach can be viewed as a simplified version of the DB theory: it retains much of the accuracy of the parent theory [87], yet avoids the computational cost of the four-point vertex function by relying only on a numerically less expensive three-point object. As a result of this

simplification, the diagrammatic structure of the self-energy and polarization operator in D-TRILEX reduces to a *GW*-like form [17, 86], which is significantly more computationally efficient than in DF, DB, or D Γ A methods, as it avoids solving the Bethe–Salpeter equation in frequency space. A rather simple form of the D-TRILEX diagrams allows one to perform feasible multi-orbital [104, 113–117] and time-dependent [118] calculations.

So far, D-TRILEX calculations have been performed only for the multi-orbital or multi-impurity reference system [17, 110]. Implementing the cluster version of the method would allow us to combine the advantages of both approaches: the exact treatment of short-range correlations via the cluster DMFT reference problem and the efficient diagrammatic description of the long-range collective electronic fluctuations with a good momentum resolution. This can be of particular importance for the low-dimensional systems, where the non-perturbative short-range correlations coexist with the long-range charge and spin fluctuations. Additionally, using the cluster reference problem would allow one to address phase transitions associated with non-local order parameters, such as the *d*-wave superconducting state. The cluster extensions of the DF [30, 72, 119–122] and TRILEX [123] methods have already been implemented. We believe that the cluster D-TRILEX approach would serve as a good alternative to these computational schemes due to a much more efficient diagrammatic structure and the absence of the Fierz ambiguity problem, respectively.

In this work, we present the cluster extension of the D-TRILEX method. In Sec. II we discuss the general formulation of the method and present the computational scheme. In Sec. III we apply our method to the one-dimensional nanoring Hubbard model. The results are benchmarked against the exact QMC solution of the problem from the Ref. [18]. In particular, we demonstrate that for metallic systems, the implemented cluster D-TRILEX approach yields significantly more accurate results for the self-energy at the Fermi energy than the much more computationally demanding parquet D Γ A approximation. Further, we discuss several periodization schemes based on the self-energy and Green’s function, and analyze how the incorporation of the inter-cluster correlations in the CDMFT scheme results in a partial restoration of translational symmetry that is absent in conventional CDMFT solutions. A summary and outlook are given in Sec. IV.

II. CLUSTER EXTENSION OF THE D-TRILEX METHOD

We start with a general action of the Hubbard model:

$$S = - \sum_{\mathbf{k}, \sigma, l} c_{\mathbf{k}\sigma l}^* \left[(i\nu + \mu) \delta_{ll'} - \varepsilon_{\mathbf{k}}^{ll'} \right] c_{\mathbf{k}\sigma l'} + \frac{1}{2} \sum_{\{\mathbf{k}\}, \mathbf{q}} \sum_{\{l\}, \{\sigma\}} U_{l_1 l_2 l_3 l_4} c_{\mathbf{k}\sigma l_1}^* c_{\mathbf{k}+\mathbf{q}, \sigma l_2} c_{\mathbf{k}'+\mathbf{q}, \sigma' l_4} c_{\mathbf{k}' \sigma' l_3}. \quad (1)$$

In this expression, $c_{\mathbf{k}\sigma l}^{(*)}$ is the Grassmann variable that describes the annihilation (creation) of an electron with momentum \mathbf{k} , fermionic Matsubara frequency ν , and spin projection

$\sigma \in \{\uparrow, \downarrow\}$. The label l numerates the orbital and the site within the unit cell. To simplify notations, we use a combined index $k \in \{\mathbf{k}, \nu\}$. The momentum \mathbf{k} arises from the translational invariance of the unit cell. $\epsilon_{\mathbf{k}}^{\text{ll}}$ is a Fourier transform of the hopping matrix and μ is the chemical potential. $U_{l_1 l_2 l_3 l_4}$ is the electron-electron interaction within the unit cell. The bosonic momentum \mathbf{q} and Matsubara frequency ω dependence is also depicted by a combined index $q \in \{\mathbf{q}, \omega\}$.

The diagrammatic expansion in dual techniques can be formulated on the basis of an arbitrary interacting reference problem [72]. The standard choice is the impurity problem obtained from the DMFT mapping of the lattice problem. Besides the single-band DMFT impurity problem, the D-TRILEX calculations have been performed only for the multi-orbital or multi-impurity reference systems [17, 110]. Cluster problem has the same algebraic structure and can, in fact, be regarded as multi-orbital system in which the orbital indices correspond to cluster sites. However, the principal difficulty is that ordinary multi-orbital single-site impurity problems employ an orthogonal local basis, so both the on-site Hamiltonian and the hybridization function are diagonal. In a cluster formulation, the inter-site hopping necessarily introduces off-diagonal matrix elements in both objects. The presence of these terms drastically complicates the numerical solution of the impurity problem and frequently results in the fermionic sign problem [42, 124, 125].

A. Diagonalization of the reference system

CDMFT maps the original lattice problem onto an impurity model of a cluster embedded in a bath described by the hybridization function Δ_{ν}^{ll} :

$$\begin{aligned} \mathcal{S}_{\text{imp}} = & \sum_{\nu, \sigma, l} c_{\nu \sigma l}^* \left[(i\nu + \mu) \delta_{\text{ll}} - \Delta_{\nu}^{\text{ll}} \right] c_{\nu \sigma l} \\ & + \sum_{\{\nu\}, \omega} \sum_{\{l\}, \{\sigma\}} U_{l_1 l_2 l_3 l_4} c_{\nu \sigma l_1}^* c_{\nu + \omega, \sigma l_2} c_{\nu' + \omega, \sigma' l_4}^* c_{\nu', \sigma' l_3}. \end{aligned} \quad (2)$$

In CDMFT, the hybridization function Δ_{ν}^{ll} becomes a matrix in the space of cluster sites $\{l, l'\}$ that in general has off-diagonal terms. In order to avoid dealing with the sign problem, let us perform a basis transformation, \mathcal{R} , to diagonalize the Hermitian matrix Δ_{ν}^{ll} :

$$\Delta_{\nu} = \mathcal{R}_{\nu}^{\dagger} D_{\nu} \mathcal{R}_{\nu}, \quad (3)$$

where D_{ν} is a diagonal matrix. This basis transformation (3) motivates the definition of new Grassmann variables:

$$\bar{c}_{\nu \sigma l}^* = \sum_{l'} c_{\nu \sigma l'}^* [\mathcal{R}_{\nu}^{\dagger}]_{l'l}, \quad \bar{c}_{\nu \sigma l} = \sum_{l'} [\mathcal{R}_{\nu}]_{ll'} c_{\nu \sigma l'}. \quad (4)$$

The rotation matrix is unitary, since the hybridization function is Hermitian, ensuring that anti-commutation relations are preserved. The impurity problem (5) becomes:

$$\begin{aligned} \mathcal{S}_{\text{imp}} = & \sum_{\nu, \sigma, l} \bar{c}_{\nu \sigma l}^* \left[i\nu + \mu - D_{\nu}^{\text{ll}} \right] \bar{c}_{\nu \sigma l} \\ & + \sum_{\{\nu\}, \omega} \sum_{\{l\}, \{\sigma\}} \mathcal{U}_{l_1 l_2 l_3 l_4}^{\nu \nu' \omega} \bar{c}_{\nu \sigma l_1}^* \bar{c}_{\nu + \omega, \sigma l_2} c_{\nu' + \omega, \sigma' l_4}^* \bar{c}_{\nu', \sigma' l_3}, \end{aligned} \quad (5)$$

where the static electron-electron interaction transforms to a three-frequency-dependent object:

$$\mathcal{U}_{l_1 l_2 l_3 l_4}^{\nu \nu' \omega} = \sum_{\{j\}} U_{j_1 j_2 j_3 j_4} [\mathcal{R}_{\nu}]_{l_1 j_1} [\mathcal{R}_{\nu + \omega}^{\dagger}]_{j_2 l_2} [\mathcal{R}_{\nu' + \omega}]_{l_4 j_4} [\mathcal{R}_{\nu'}^{\dagger}]_{j_3 l_3}. \quad (6)$$

Handling such a complex interaction is beyond the capabilities of existing impurity solvers. Thus, neither option provides a viable solution: avoiding the sign problem leads to an intractable interaction, while keeping the interaction static reintroduces the sign problem.

To address this problem, in Refs. [124, 125] the author showed that for different types of clusters there exists a static (frequency-independent) transformation to an “optimal” single-particle basis for which the sign problem decreases significantly. Yet, the sign problem cannot be completely removed and still scales exponentially with the inverse of the temperature.

In our work, we follow a similar idea and perform a basis transformation to diagonalize the local part of the single-particle Hamiltonian:

$$\bar{\epsilon}_K = \mathcal{R} \left[\sum_K \epsilon_K \right] \mathcal{R}^{\dagger}. \quad (7)$$

This transformation minimizes the off-diagonal components of the hybridization function, as can be seen by applying the basis transformation directly to the hybridization function (see Appendix A for a detailed derivation):

$$\bar{\Delta}_{\nu} = \mathcal{R} \Delta_{\nu} \mathcal{R}^{\dagger} = \mathcal{R} \left[\sum_K \epsilon_K \right] \mathcal{R}^{\dagger} + \mathcal{O} \left(\sum_K \mathcal{R} \frac{(\epsilon_K + \Sigma_{\nu}^{\text{imp}})^2}{i\nu + \mu} \mathcal{R}^{\dagger} \right), \quad (8)$$

where $\Sigma_{\nu}^{\text{imp}}$ is the self-energy of the cluster impurity problem. Importantly, this basis transformation is momentum-independent, which helps to preserve the causality of the cluster method [21, 22, 126]. However, the off-diagonal components of the hybridization function cannot be fully eliminated. In our approach, we take a further step by removing these off-diagonal terms through the flexibility in choosing the reference system for the dual diagrammatic expansion [72]. In dual approaches, the impurity problem (5) is separated from the original lattice action (1) by adding and subtracting the hybridization function Δ_{ν}^{ll} , which may be chosen arbitrarily in the band space $\{l, l'\}$ (see, e.g., Ref. [17]). After performing the basis transformation \mathcal{R} that diagonalizes the local part of the single-particle Hamiltonian $\epsilon_{\mathbf{k}}$, we choose to work with a diagonal hybridization function, Δ_{ν}^{ll} . The off-diagonal components of the cluster self-energy are then generated via the diagrammatic expansion, which accounts for both momentum-independent and momentum-dependent contributions beyond the impurity self-energy $\Sigma_{\nu, \text{ll}}^{\text{imp}}$. The proposed scheme is general and can be applied to arbitrary cluster problems. In what follows, we demonstrate its applicability using the one-dimensional nano-ring Hubbard model with a dimer reference system as a representative example.

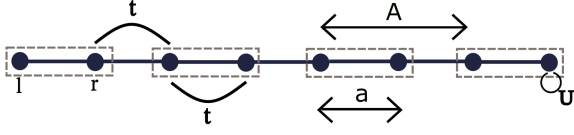


FIG. 1. Schematic representation of the one-dimensional Hubbard model. The lattice is tiled by identical two-site clusters, indicated by dashed boxes, consisting of the “left” (l) and “right” (r) sites. The nearest-neighbor hopping amplitude t is considered the same within and between the clusters. The electrons interact via the on-site Coulomb repulsion U . The distance between adjacent clusters is $A = 2a$, i.e., twice the lattice constant a .

B. Basis transformation for the 1D Hubbard model

We start with the one-dimensional Hubbard Hamiltonian:

$$H = -t \sum_{j,\tau,\sigma} c_{j,\sigma}^\dagger c_{j+\tau,\sigma} + U \sum_j n_{j\uparrow} n_{j\downarrow}, \quad (9)$$

where j labels the atomic position, $\tau = \pm 1$ denotes the nearest-neighbor site position difference, t denotes the nearest-neighbor hopping integral, $c_{j,\sigma}^{(\dagger)}$ is the annihilation (creation) operator for an electron at site j , with spin σ ; $n_{j,\sigma} = c_{j,\sigma}^\dagger c_{j,\sigma}$ is the density operator. For the remainder of this work, we set $t = 1$ and use it as the energy unit. The chemical potential is set to $\mu = U/2$ so that the system is at half filling.

In the case of a two-site cluster formulation of the problem one can introduce the spinors:

$$C_l = \begin{pmatrix} l_l^\dagger \\ r_l^\dagger \end{pmatrix} \text{ and } C_l^\dagger = \begin{pmatrix} l_l^\dagger & r_l^\dagger \end{pmatrix}, \quad (10)$$

where $l_l^{(\dagger)}$ and $r_l^{(\dagger)}$ are the annihilation (creation) operators for the electron on the left and right sites in the cluster l , respectively (see Fig. 1). The local part of the single-particle Hamiltonian becomes:

$$H_0^{\text{loc}} = - \sum_l C_l^\dagger \begin{pmatrix} 0 & t \\ t & 0 \end{pmatrix} C_l. \quad (11)$$

It can be diagonalized by the following transformation to the bonding-antibonding basis:

$$\mathcal{R} = \frac{1}{\sqrt{2}} \begin{pmatrix} 1 & 1 \\ 1 & -1 \end{pmatrix}. \quad (12)$$

The full single-particle Hamiltonian has the following form:

$$\begin{aligned} H_0 &= - \sum_l C_l^\dagger \left\{ \begin{pmatrix} 0 & t \\ t & 0 \end{pmatrix} C_l + \begin{pmatrix} 0 & t \\ 0 & 0 \end{pmatrix} C_{l-1} + \begin{pmatrix} 0 & 0 \\ t & 0 \end{pmatrix} C_{l+1} \right\} \\ &= - \frac{t}{N_K} \sum_K C_K^\dagger \begin{pmatrix} 0 & 1 + e^{-iAK} \\ 1 + e^{iAK} & 0 \end{pmatrix} C_K, \end{aligned} \quad (13)$$

where N_K is the number of K -points in the reduced BZ, $A = 2a$ is the distance in real space between the neighboring clusters (vector of translation), and a is the lattice constant.

Upon the basis transformation, the single-particle Hamiltonian becomes:

$$\bar{H}_0 = \frac{1}{N_K} \sum_K \bar{C}_K^\dagger \bar{\varepsilon}_K \bar{C}_K, \quad (14)$$

where:

$$\bar{\varepsilon}_K = -t \begin{pmatrix} 1 + \cos(AK) & i \sin(AK) \\ -i \sin(AK) & -1 - \cos(AK) \end{pmatrix} \quad (15)$$

and we also introduced a new spinor

$$\bar{C} = \mathcal{R} C = \frac{1}{\sqrt{2}} \left\{ \begin{pmatrix} 1 \\ 1 \end{pmatrix} l + \begin{pmatrix} 1 \\ -1 \end{pmatrix} r \right\} = \begin{pmatrix} a \\ b \end{pmatrix}. \quad (16)$$

The interaction part of the Hamiltonian:

$$H_U = U \sum_j n_{j\uparrow} n_{j\downarrow} \quad (17)$$

transforms to the Kanamori-like form [127] ($m, m' \in \{a, b\}$)

$$\begin{aligned} \bar{H}_U &= \frac{1}{2} \sum_{l,m} \mathcal{U} n_{l,\sigma}^m n_{l,\sigma'}^m + \frac{1}{2} \sum_{l,\sigma\sigma'} (\mathcal{U}' - \mathcal{J} \delta_{\sigma\sigma'}) n_{l,\sigma}^m n_{l,\sigma'}^{m'} \\ &\quad - \mathcal{J} \sum_l (a_{l\uparrow}^\dagger a_{l\downarrow} b_{l\downarrow}^\dagger b_{l\uparrow} + b_{l\uparrow}^\dagger b_{l\downarrow} a_{l\downarrow}^\dagger a_{l\uparrow}) \\ &\quad + \mathcal{J} \sum_l (a_{l\uparrow}^\dagger a_{l\downarrow}^\dagger b_{l\downarrow} b_{l\uparrow} + b_{l\uparrow}^\dagger b_{l\downarrow}^\dagger a_{l\downarrow} a_{l\uparrow}) \end{aligned} \quad (18)$$

with an effective intra- (\mathcal{U}) and inter-band (\mathcal{U}') Coulomb interactions and Hund's exchange coupling (\mathcal{J}) equal to $\mathcal{U} = \mathcal{U}' = \mathcal{J} = U/2$.

C. Computational scheme

The lattice problem (9) in the bonding-antibonding basis

$$\bar{H} = \bar{H}_0 + \bar{H}_U \quad (19)$$

is solved using the multi-band D-TRILEX approach described in Ref. [17]. Below we provide the key steps of the computational workflow:

1. DMFT calculation:

a. Diagonalizing the local part of the single-particle Hamiltonian:

Find the basis transformation \mathcal{R} that diagonalizes the local part of the single-particle Hamiltonian.

b. Basis transformation:

Perform the basis transformation \mathcal{R} for the full Hamiltonian (9).

c. DMFT solution:

Solve the transformed Hamiltonian (19) using DMFT with the diagonal hybridization function Δ_V^H . In this work, the DMFT solution is obtained using the w2dynamics package [128].

d. Evaluating impurity quantities:

Once DMFT self-consistency is reached, the impurity Green's

function g_ν , the self-energy Σ_ν^{imp} , the fermionic hybridization function Δ_ν , the charge ($\varsigma = \text{ch}$) and spin ($\varsigma = \text{sp} \in \{x, y, z\}$) susceptibilities χ_ω^ς , the polarization operator $\Pi_{\text{imp}\omega}^\varsigma$ and the three-point vertex functions $\Lambda_{\nu\omega}^\varsigma$, needed for the diagrammatic part of the D-TRILEX scheme, are calculated from the converged DMFT solution. Here, ν and ω refer respectively to fermionic and bosonic Matsubara frequencies.

2. Self-consistent calculation of D-TRILEX diagrams:

The self-consistent calculation of single- and two- particle quantities in the dual space goes as follows:

a. Evaluating bare propagators:

The output of the DMFT impurity problem is used to construct building blocks for the D-TRILEX diagrammatic expansion.

The bare dual Green's function $\tilde{G}_{K\nu}^{\text{imp}} = \hat{G}_{K\nu}^{\text{imp}} - \delta_{ll'} g_\nu^{\text{imp}}$ corresponds to the difference between the DMFT \hat{G} and impurity g Green's functions, and thus is dressed only in the impurity self-energy Σ^{imp} :

$$[\hat{G}_{K\nu}]_{ll'}^{-1} = [G_{K\nu}^0]_{ll'}^{-1} - \delta_{ll'} \Sigma_{\nu, ll}^{\text{imp}}. \quad (20)$$

In this expression, G_0^{-1} is the inverse of the bare lattice Green's function defined as:

$$[G_{K\nu}^0]_{ll'}^{-1} = \delta_{ll'} (i\nu + \mu) - \bar{\epsilon}_K^{\text{imp}}. \quad (21)$$

The bare dual bosonic propagator (renormalized interaction) $\tilde{W}_{Q,\omega,\varsigma}^{l_1 l_2; l_3 l_4} = \hat{W}_{Q,\omega,\varsigma}^{l_1 l_2; l_3 l_4} - \frac{1}{2} U_\varsigma^{l_1 l_2 l_3 l_4}$ is the bare interaction U^ς renormalized by the local polarization operator of the impurity problem $\Pi_{\text{imp}}^\varsigma$ in the charge and spin channels:

$$[\hat{W}_{Q,\omega,\varsigma}]_{l_1 l_2; l_3 l_4}^{-1} = [U^\varsigma]_{l_1 l_2; l_3 l_4}^{-1} - \Pi_{\text{imp}\omega,\varsigma}^{l_1 l_2; l_3 l_4}. \quad (22)$$

Here, $\frac{1}{2} U^\varsigma$ is subtracted from \hat{W}^ς in order to prevent double counting of the bare interaction between different channels. Q denotes the bosonic momentum in the reduced BZ.

b. Computing the dual polarization operator:

The dual polarization operator $\tilde{\Pi}^\varsigma$ in the charge and spin channel is expressed in terms of the dual Green's function \tilde{G} and the vertex function Λ^ς :

$$\tilde{\Pi}_{Q,\omega,\varsigma}^{l_1 l_2; l_7 l_8} = 2 \sum_{\mathbf{k}, \nu, \{l\}} \Lambda_{\nu+\omega, -\omega, \varsigma}^{l_4, l_3; l_2 l_1} \tilde{G}_{K, \nu}^{l_3 l_5} \tilde{G}_{K+Q, \nu+\omega}^{l_6 l_4} \Lambda_{\nu, \omega, \varsigma}^{l_5, l_6; l_7 l_8}. \quad (23)$$

c. Computing the dressed dual renormalized interaction:

The dressed dual renormalized interaction \tilde{W}^ς in the charge and spin channel is calculated using the following expression:

$$[\tilde{W}_{Q,\omega,\varsigma}]_{l_1 l_2; l_3 l_4}^{-1} = [\tilde{W}_{Q,\omega,\varsigma}]_{l_1 l_2; l_3 l_4}^{-1} - \tilde{\Pi}_{Q,\omega,\varsigma}^{l_1 l_2; l_3 l_4}. \quad (24)$$

d. Computing the dual self-energy:

The dual self-energy $\tilde{\Sigma}$ is expressed in terms of the dual Green's function \tilde{G} , the renormalized interaction \tilde{W}^ς , and the vertex function Λ^ς :

$$\begin{aligned} \tilde{\Sigma}_{K\nu}^{l_1 l_7} = & 2 \sum_{K', \nu', \{l\}} \Lambda_{\nu, \omega=0, \text{ch}}^{l_1, l_7; l_3 l_4} \tilde{W}_{Q=0, \omega=0, \text{ch}}^{l_3 l_4; l_5 l_6} \Lambda_{\nu', \omega=0, \text{ch}}^{l_8, l_2; l_6 l_5} \tilde{G}_{K' \nu'}^{l_2 l_8} \\ & - \sum_{\mathbf{q}, \omega, \varsigma, \{l\}} \Lambda_{\nu, \omega, \varsigma}^{l_1, l_2; l_3 l_4} \tilde{G}_{K+Q, \nu+\omega}^{l_3 l_4; l_5 l_6} \tilde{W}_{Q, \omega, \varsigma}^{l_5 l_6; l_7 l_8} \Lambda_{\nu+\omega, -\omega, \varsigma}^{l_8, l_7; l_6 l_5}. \end{aligned} \quad (25)$$

e. Computing the dressed dual Green's function:

The dressed dual Green's function \tilde{G} is calculated using the following expression:

$$[\tilde{G}_{K\nu}]_{ll'}^{-1} = [\tilde{G}_{K\nu}]_{ll'}^{-1} - \tilde{\Sigma}_{K\nu}^{\text{imp}}. \quad (26)$$

f. Go back to step b. and iterate until convergence.

3. Evaluating lattice quantities:

a. Evaluating the lattice self-energy and Green's function:

The lattice self-energy $\bar{\Sigma}$ is obtained from the exact relation:

$$\bar{\Sigma}_{K\nu}^{\text{imp}} = \delta_{ll'} \Sigma_{\nu, ll}^{\text{imp}} + \sum_{l_1} \tilde{\Sigma}_{K\nu}^{ll_1} [\mathbb{1} + g_\nu \cdot \tilde{\Sigma}_{K\nu}]_{l_1 l'}^{-1}. \quad (27)$$

The lattice Green's function is then obtained as:

$$[\bar{G}_{K\nu}]_{ll'}^{-1} = [G_{K\nu}^0]_{ll'}^{-1} - \bar{\Sigma}_{K\nu}^{\text{imp}}. \quad (28)$$

b. Transforming lattice quantities to the original basis:

In order to obtain the self-energy and the Green's function in the original basis, we perform the following transformation:

$$O_{K\nu} = \mathcal{R}^\dagger \bar{O}_{K\nu} \mathcal{R} \quad (29)$$

with $O_{K\nu}$ being the lattice self-energy $\Sigma_{K\nu}$ or the Green's function $G_{K\nu}$.

c. Periodization from the cluster to single-site form:

To obtain the lattice self-energy and Green's function corresponding to the single-site unit cell from the cluster quantities, we perform the following periodization step by imposing the translational invariance of the original lattice problem:

$$O_{k\nu}^{\text{latt}} = \mathcal{L}_k [O_{k\nu}^{\text{imp}}] = \frac{1}{N_c} \sum_{l'} e^{ik(r_l - r_{l'})} O_{k\nu}^{\text{imp}}, \quad (30)$$

where r_l is the position of the l -th atom in the unit cell and k corresponds to the original (extended) BZ. In the dimer case, this relation reduces to

$$O_{k\nu}^{\text{latt}} = \frac{1}{2} (O_{k\nu}^{11} + O_{k\nu}^{22}) + \text{Re } O_{k\nu}^{12} \cos(ka) + \text{Im } O_{k\nu}^{12} \sin(ka). \quad (31)$$

The quantity $O_{k\nu}^{\text{imp}}$ in the extended BZ can be obtained from the cluster quantity $O_{K\nu}^{\text{imp}}$ in the reduced BZ using the periodicity in momentum space.

III. RESULTS

To demonstrate the performance of the D-TRILEX method, we apply it to the one-dimensional nano-ring Hubbard model. We focus on periodic chains with $N_c = 4, 6$, and 8 lattice sites, for which results can be directly compared to the exact Hirsch-Fye QMC solution and to the more involved DfA method in the ladder and parquet implementations, for which the data are available from Ref. [18]. For consistency with that work, all calculations are performed for $t = 1$, $U = 2$, and inverse temperature $\beta = 10$.

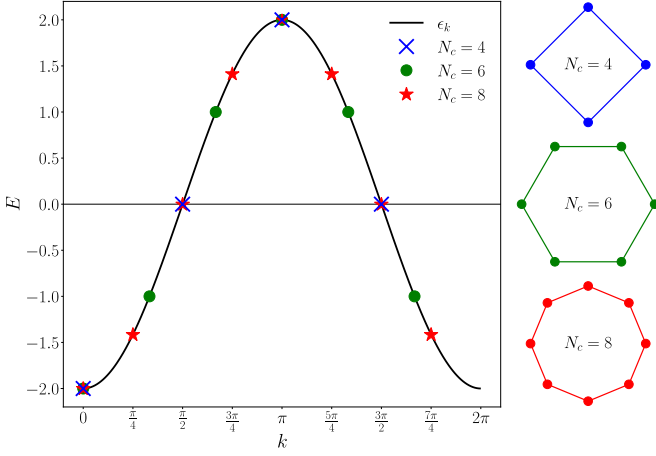


FIG. 2. The left panel shows the electronic spectral function ϵ_k along the first Brillouin zone (lattice constant $a = 1$). The dashed curve represents the dispersion of an infinite one-dimensional chain, whereas the discrete symbols correspond to the finite number of lattice sites N_c . The right column depicts the ring geometries: a four-site (blue, top), a six-site (green, middle), and an eight-site (red, bottom) rings. In the dispersion plot their spectra are indicated by blue crosses, green circles, and red stars, respectively.

A. Insulating system, $N = 6$

We refer to the configuration with $N_c = 6$ sites as an insulating system, since its non-interacting spectral function exhibits an energy gap separating the occupied states at $k = 0, \pi/3, 5\pi/3$ from the unoccupied states at $k = 2\pi/3, \pi, 4\pi/3$. This behavior is illustrated in Fig. 2, where the $N_c = 6$ case is shown in green.

In Fig. 3 we plot the imaginary part of the lattice self-energy

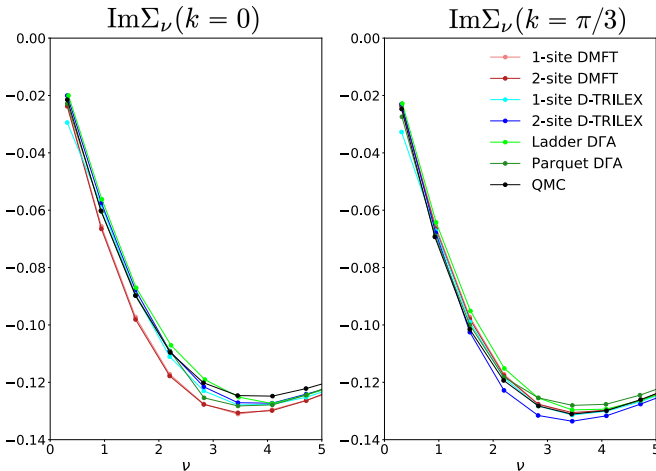


FIG. 3. The imaginary part of the self-energy calculated as a function of Matsubara frequency ν at two momenta $k = 0$ (left) and $k = \pi/3$ (right). The results are obtained for the case of $N_c = 6$ at $U = 2$ and $\beta = 10$ using different methods indicated in the legend. The ladder DΓA, parquet DΓA, and exact QMC results are taken from Ref. [18].

calculated at $k = 0$ (a) and $k = \pi/3$ (b) momenta as a function of Matsubara frequency ν . The results are obtained using the single-site DMFT (light red), two-site cluster DMFT (dark red), single-site D-TRILEX (light blue), two-site cluster D-TRILEX (dark blue) and are compared with the ladder DΓA (light green), parquet DΓA (dark green) and QMC (black) data of Ref. [18]. The two-site cluster DMFT and D-TRILEX self-energies are periodized from the cluster space corresponding to the reduced BZ to the single-site form corresponding to the extended BZ using Eq. (30). The small momentum-dependence of the imaginary part of the self-energy, that can be seen in Fig. 3, allows for the DMFT results to be close to the exact QMC result. Both DΓA and D-TRILEX methods improve upon DMFT and reproduce a slight change of the self-energy between the $k = 0$ and $k = \pi/3$ points. We observe that the single-site D-TRILEX calculations slightly overestimate the self-energy at low frequencies, but the cluster extension of the method cures this problem and is in a very good agreement with the QMC result. Overall, we find that the imaginary part of the self-energy is reproduced with good accuracy by all methods in the insulating case of $N_c = 6$.

In contrast, the real part of the self-energy, shown in Fig. 4, exhibits more differences among the considered methods. At the both $k = 0$ and $k = \pi/3$ momenta the single-site D-TRILEX displays a nearly constant offset of comparable magnitude with respect to the exact QMC result, showing that the discrepancy is approximately momentum-independent. The cluster D-TRILEX improves the real part of the self-energy at $k = \pi/3$ momentum close to the Fermi level, but the self-energy at the edge of the BZ ($k = 0$) become less accurate. Interestingly, the real part of the cluster D-TRILEX self-energy at $k = 0$ is very similar to that obtained from cluster DMFT. We note that at $k = 0$, the dominant contribution to $\text{Re } \Sigma$ originates from the off-diagonal

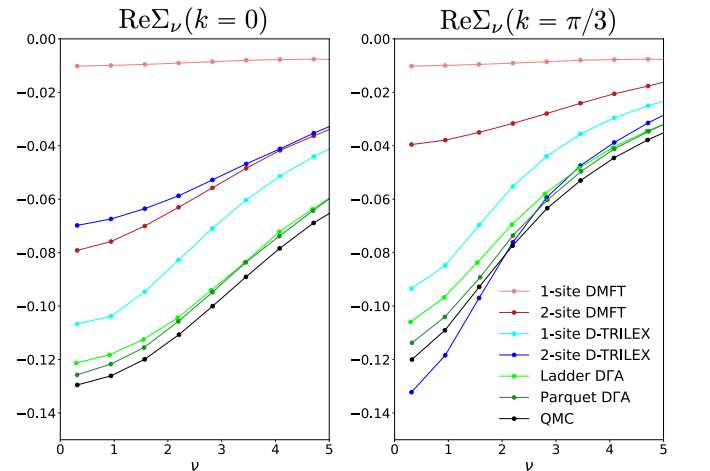


FIG. 4. The real part of the self-energy calculated as a function of Matsubara frequency ν at two momenta $k = 0$ (left) and $k = \pi/3$ (right). The results are obtained for the case of $N_c = 6$ at $U = 2$ and $\beta = 10$ using different methods indicated in the legend. The ladder DΓA, parquet DΓA, and exact QMC results are taken from Ref. [18].

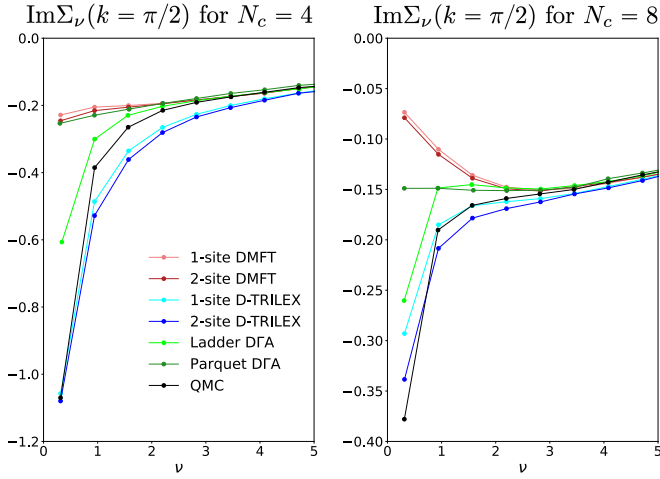


FIG. 5. The imaginary part of the self-energy as a function of Matsubara frequency ν at momentum $k = \pi/2$ for the systems with $N_c = 4$ (left) and $N_c = 8$ (right). All results are computed at $U = 2$ and $\beta = 10$ using the methods indicated in the legend. The ladder DFA, parquet DFA, and exact QMC results are taken from Ref. [18].

cluster term Σ_{12} (see Eq. (31)). The similarity between the cluster DMFT and D-TRILEX results suggests that the non-perturbative short-range correlation effects captured by the reference system contribute significantly to Σ_{12} . In the insulating case, non-local collective electronic fluctuations are expected to be weak, and therefore the additional perturbative diagrammatic corrections have only a minor impact on Σ_{12} . We also note that, although the D-TRILEX results for the real part of the self-energy in the $N_c = 6$ case are less accurate than those of DFA, the self-energy itself remains very small compared to the electronic dispersion, $|\text{Re } \Sigma| \ll |\epsilon_k|$. Therefore, the observed discrepancy is not expected to have a significant impact.

B. Metallic systems, $N = 4, 8$

In the cases of $N_c = 4$ and $N_c = 8$, which we refer to as metallic systems, the non-interacting spectral function exhibits a doubly degenerate state at the Fermi level, corresponding to the momenta $k = \pi/2$ and $k = 3\pi/2$. This behavior is illustrated by the blue and red colors in Fig. 2, respectively. This suggests that the self-energies at non-equivalent k -points may exhibit significant momentum-dependent variation, particularly when comparing values at the Fermi energy to those further away from it. Single-site DMFT is not able to reproduce the momentum dependence of the self-energy, and more elaborate methods are required to capture these effects.

In Fig. 5 we show the imaginary part of the self-energy calculated at $k = \pi/2$ as a function of frequency for the case of $N_c = 4$ (left) and $N_c = 8$ (left). Note, that $\text{Re } \Sigma(k = \pi/2) = 0$ in our case. This k -point corresponds to the Fermi energy, and the self-energy at $k = \pi/2$ is much larger than the one obtained at $k = 0$ (see Fig. 6). First, the exact $\text{Im } \Sigma(k = \pi/2)$ provided

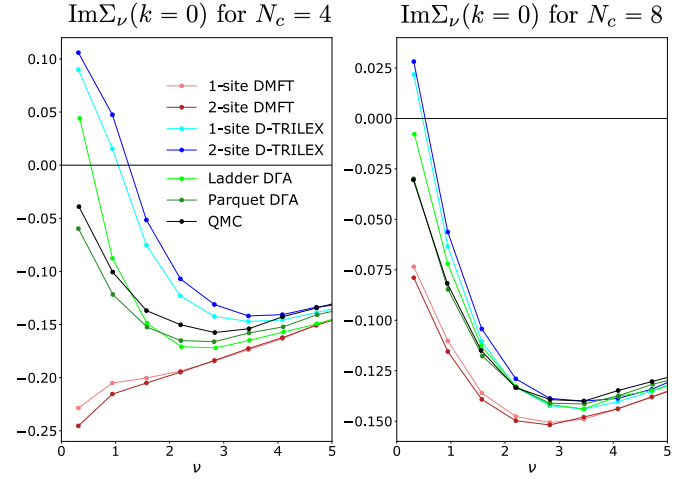


FIG. 6. The imaginary part of the self-energy as a function of Matsubara frequency ν at momentum $k = 0$ for lattices with $N_c = 4$ (left) and $N_c = 8$ (right). All curves are calculated at $U = 2$ and $\beta = 10$ using the methods specified in the legend. The ladder DFA, parquet DFA, and exact QMC results are taken from Ref. [18].

by QMC for both $N_c = 4$ and $N_c = 8$ cases shows an insulating (divergent as $\nu \rightarrow 0$) behavior. Interestingly, the cluster DMFT result fails to reproduce this behavior and nearly coincides with the single-site DMFT result. This indicates that long-range collective electronic fluctuations play a crucial role in the metallic case, particularly at the Fermi energy. Among all considered approaches, D-TRILEX provides the most accurate result for the self-energy at $k = \pi/2$. At $N_c = 4$, the single-site and cluster D-TRILEX results nearly coincide, with the cluster version being closer to the exact result at the lowest Matsubara frequency, while the single-site approximation is more accurate at higher frequencies. This trend persists for $N_c = 8$, although the difference between the single-site and cluster D-TRILEX results becomes more pronounced. The ladder DFA captures the insulating behavior of the self-energy but is substantially less accurate than both versions of D-TRILEX. Surprisingly, we find that although the parquet DFA is a diagrammatic extension of the ladder version, it performs significantly worse: it fails to capture the insulating behavior of the self-energy and even remains at the level of DMFT for $N_c = 4$. Ref. [18] attributes the better performance of ladder DFA at $k = \pi/2$ to the so-called λ -correction, arguing that it effectively emulates an outer self-consistency by modifying the impurity problem. Our comparison challenges this interpretation, since the single-site D-TRILEX approach, which features a similar (ladder-like) diagrammatic structure, uses the same DMFT impurity problem as a reference for the diagrammatic expansion, and also does not perform an outer self-consistency loop, yet achieves better accuracy without employing the λ -correction.

At the Brillouin zone center, $k = 0$, the parquet DFA provides the most accurate description of both the imaginary (Fig. 6) and real (Fig. 7) parts of the self-energy, while both DMFT versions are the least accurate. We note that $\text{Im } \Sigma(k = 0)$ for $N_c = 4$ predicted by the single-site and cluster

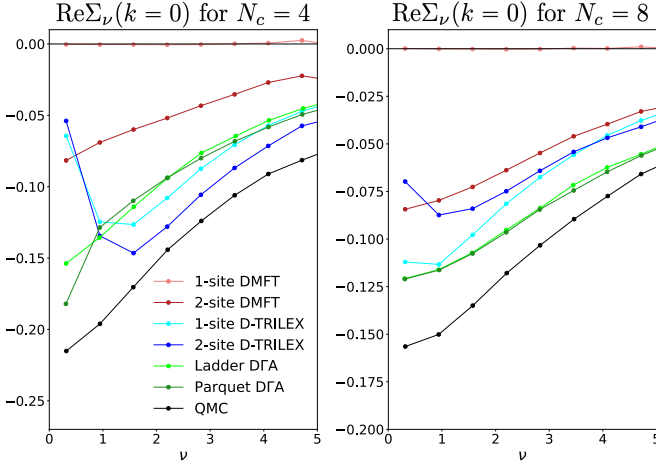


FIG. 7. The real part of the self-energy as a function of Matsubara frequency ν at momentum $k = 0$ for lattices with $N_c = 4$ (left) and $N_c = 8$ (right). All results are computed at $U = 2$ and $\beta = 10$ using the methods indicated in the legend. The ladder DGA, parquet DGA, and exact QMC results are taken from Ref. [18]

D-TRILEX approaches shows a non-causal behavior for the two lowest Matsubara frequencies. The anomaly carries over to the real part of the self-energy, where the first two Matsubara points deviate strongly from the exact trend. This behavior improves with increasing the number of lattice sites to $N_c = 8$, but the imaginary part of the D-TRILEX self-energy still remains positive at the lowest Matsubara frequency. A similar behavior for $\text{Im}\Sigma(k=0)$ is also found in Ref. [18] for the ladder DGA approach in the case of $N_c = 4$ and is attributed to the neglect of particle-particle diagrams inherent in the particle-hole ladder approximation. The current D-TRILEX implementation also omits particle-particle correlations. However, the fact that the cluster extension of the single-site D-TRILEX does not lead to significant improvements suggests that the missing diagrammatic contributions are likely long-ranged and go beyond a perturbative ladder-like approximation. Furthermore, Fig. 8 demonstrates that the non-causal behavior can be cured by increasing the number of lattice sites to $N_c = 16$, and the imaginary part of the single-site D-TRILEX self-energy calculated at $k = 0$ for $N_c = 32$ nearly coincides with the one obtained for $N_c = 16$. This result suggests that increasing the system size reduces the impact of correlations beyond the two-particle level that are neglected in the D-TRILEX and ladder DGA approaches.

In general, as in the insulating $N_c = 6$ case, the real part of the self-energy away from the Fermi energy remains relatively small compared to the electronic dispersion, $|\text{Re}\Sigma(k=0)| \ll |\epsilon_k|$, so discrepancies with the exact QMC results are not expected to be significant for describing the electronic properties of the system. At the same time, we again observe a strong similarity between the cluster DMFT and D-TRILEX results, particularly in the $N_c = 8$ case. This behavior can be attributed to the fact that at $k = 0$, the real part of the self-energy (31):

$$\text{Re}\Sigma_{k=0,\nu} = \frac{1}{2}\text{Re}\left[\Sigma_{k=0,\nu}^{11} + \Sigma_{k=0,\nu}^{22}\right] + \text{Re}\Sigma_{k=0,\nu}^{12} \quad (32)$$

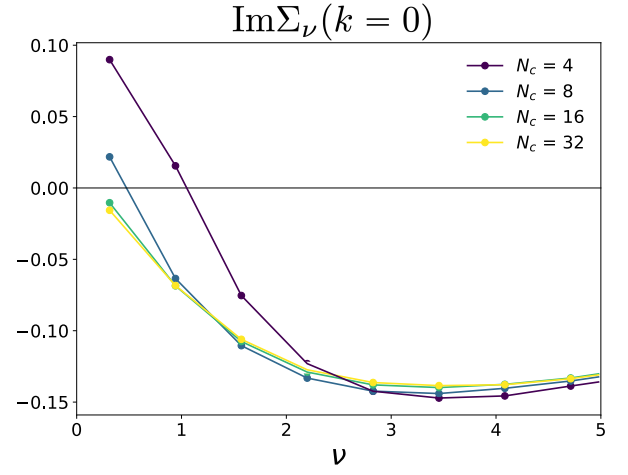


FIG. 8. Evolution of the imaginary part of the self-energy calculated at $k = 0$, $U = 2$, and $\beta = 10$ for different number of lattice sites $N_c = 4, 8, 16$, and 32 using the single-site D-TRILEX approach.

is dominated by the off-diagonal cluster component $\text{Re}\Sigma^{12}$, which primarily arises from the non-perturbative short-range correlations captured by the reference system. The additional perturbative diagrammatic corrections to both $\text{Re}\Sigma^{11}$ and $\text{Re}\Sigma^{12}$ are not strong enough to significantly alter the total $\text{Re}\Sigma(k=0)$ (see Fig. 7). The imaginary part of $\Sigma(k=0)$ originates only from the diagonal parts of the cluster self-energy:

$$\text{Im}\Sigma_{k=0,\nu} = \frac{1}{2}\text{Im}\left[\Sigma_{k=0,\nu}^{11} + \Sigma_{k=0,\nu}^{22}\right]. \quad (33)$$

In this case, the diagrammatic contributions do not compete with the non-perturbative effects, resulting in better agreement with the exact QMC result (see Fig. 6). However, at this k -point and for small cluster sizes, the correlation effects may exhibit a more intricate structure than what can be captured by simple two-particle ladder-like excitations, as discussed above. Finally, at $k = \pi/2$ the imaginary part of the lattice self-energy reads:

$$\text{Im}\Sigma_{k=\pi/2,\nu} = \frac{1}{2}\text{Im}\left[\Sigma_{k=\pi/2,\nu}^{11} + \Sigma_{k=\pi/2,\nu}^{22}\right]. \quad (34)$$

At this k -point, which corresponds to the Fermi level, particle-hole fluctuations are strong, and accounting for them via the ladder-type diagrams included in D-TRILEX substantially improves the self-energy, as demonstrated in Fig. 5.

C. Periodization and its impact on the lattice self-energy

Let us compare two choices for the periodization of the cluster self-energy (30): (i) applying the operation \mathcal{L}_k to the self-energy, which is proportional to the inverse of the Green's function, i.e., to G^{-1} , and (ii) applying it to the Green's function G and then computing the self-energy from the periodized Green's function by inverting the Dyson equation. Since \mathcal{L}_k is a linear operation while matrix inversion is not, the two proce-

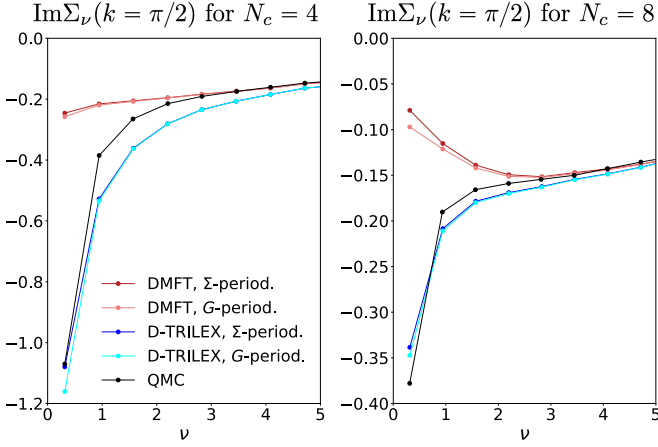


FIG. 9. The imaginary part of the lattice self-energy obtained at $k = \pi/2$ from the cluster DMFT (red colors) and cluster D-TRILEX (blue colors) methods using Σ - (light colors) and G - (dark colors) periodization schemes. The black curve corresponds to the exact QMC result taken from Ref. [18].

dures may yield different results within approximate methods:

$$(i) \Sigma_{kv}^{\text{latt}} = \mathcal{L}_k[\mathbb{1}(iv + \mu)] - \mathcal{L}_k[\varepsilon_k''] - \mathcal{L}_k[G_{kv}^{-1}] \\ = iv + \mu - \varepsilon_k - \mathcal{L}_k[G_{kv}^{-1}], \quad (35)$$

$$(ii) \Sigma_{kv}^{\text{latt}} = iv + \mu - \varepsilon_k - (\mathcal{L}_k[G_{kv}])^{-1}, \quad (36)$$

where ε_k'' is the cluster version of the original dispersion ε_k . In the following, we refer to Eq. (35) and Eq. (36) as the Σ - and G -periodization schemes, respectively.

In the case of the two-site cluster, the difference between the Σ - and G -periodization schemes can be obtained analytically. In the particle-hole-symmetric case the two-site cluster Green function reduces to:

$$G_{Kv} = \begin{pmatrix} G_{Kv}^{11} & G_{Kv}^{12} \\ G_{Kv}^{12} & G_{Kv}^{11} \end{pmatrix}, \quad (37)$$

where $G_{Kv}^{11} \in \mathbb{C}$, and $G_{Kv}^{12} \in \mathbb{R}$. The difference between the two periodization schemes for the self-energy becomes:

$$\tilde{\Sigma}_{kv}^{(ii)} - \Sigma_{kv}^{(i)} = (\mathcal{L}_k[G_{kv}])^{-1} - \mathcal{L}_k[G_{kv}^{-1}] \quad (38)$$

$$= \frac{(G_{kv}^{12})^2 \sin^2(ka)}{\left[(G_{kv}^{12})^2 - (G_{kv}^{11})^2\right] [G_{kv}^{11} + G_{kv}^{12} \cos(ka)]}. \quad (39)$$

Therefore, the two periodization schemes give identical results at $k = 0$ and is the largest at $ka = \pi/2$, i.e. at the Fermi energy.

Figure 9 compares the imaginary part of the self-energy obtained at $k = \pi/2$ ($a = 1$) using the Σ - and G -periodization schemes for $N_c = 4$ (left) and $N_c = 8$ (right) lattice sites. We find, that the two results calculated within the cluster DMFT scheme are already rather close to each other and become even closer in the cluster D-TRILEX approach. The discrepancy between the two periodization schemes in D-TRILEX

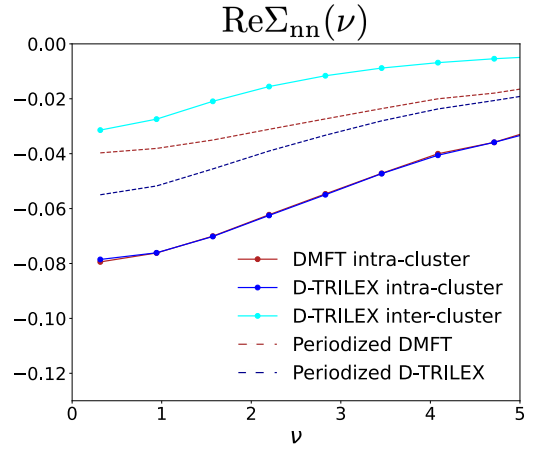


FIG. 10. The real part of the lattice self-energy between the neighboring lattice sites calculated for the case of $N_c = 8$ as a function of Matsubara frequency ν . The results are obtained for the intra-cluster DMFT (dark red), periodized DMFT (dashed red), inter-cluster D-TRILEX (light blue), intra-cluster D-TRILEX (dark blue), and periodized D-TRILEX (dashed blue) self-energies.

are only noticeable at the lowest Matsubara frequency, and the agreement improves with increasing the number of lattice sites from $N_c = 4$ to $N_c = 8$.

D. Removing off-diagonal terms from the hybridization and partial restoration of the translation invariance

Let us first justify the neglect of the off-diagonal contributions to the hybridization function. We perform CDMFT calculations for the two-site cluster impurity problem using the w2dynamics package [128], which allows inclusion of the off-diagonal hybridization in the calculation of single-particle quantities. By carrying out CDMFT with the full hybridization function, we find that transforming the two-site cluster to the bonding-antibonding basis not only eliminates the fermionic sign problem but is also well justified numerically, as the off-diagonal hybridization components remain below the numerical noise across the entire explored parameter range.

Let us now analysis if the diagrammatic contributions introduced beyond CDMFT within the cluster D-TRILEX scheme are able to, at least partially, restore the translational symmetry that got broken by introducing the cluster reference systems at the CDMFT step. To this aim, in Fig. 10 we plot the inter- and intra-cluster self-energies corresponding to the nearest-neighbor lattice sites in real space for the case of $N_c = 8$ lattice sites. In a perfectly translationally invariant system these two self-energies should be identical, i.e. $\Sigma_v^{\text{intra}} = \Sigma_v^{\text{inter}}$, and also equal to a periodized self-energy between the neighboring sites. The difference between these quantities therefore provides a convenient metric for the degree to which translational symmetry is broken.

In CDMFT the inter-cluster self-energy is identically zero. For this reason, the intra-cluster (solid red line) self-energy is

far from the periodized one depicted by the dashed red line. In the cluster D-TRILEX approach, the inter-cluster contribution to the self-energy (light blue line) is generated diagrammatically, but it is still substantially different from the intra-cluster (dark blue) and periodized (dashed blue) self-energies. The discrepancy between these different self-energies decreases in D-TRILEX compared to DMFT, which is already a good step in the direction of restoring the translational invariance. Remarkably, Fig. 10 clearly shows that the intra-cluster self-energies provided by the DMFT and D-TRILEX methods lie almost on top of each other. This close agreement can be explained by the fact that the correlations between the neighboring lattice sites in this small-scale one-dimensional system are strong and non-perturbative in nature, which is accounted for by the cluster impurity problem, as discussed above. Additional inclusion of perturbative particle-hole ladder-type contributions within D-TRILEX is not able to substantially change the intra-cluster self-energy (light blue). In this regard, the diagrammatic contribution to the inter-cluster self-energy (dark blue) is such that the periodized self-energy (dashed blue) is in a good agreement with the exact result, as demonstrated above. Therefore, we argue that the CDMFT starting point for the diagrammatic expansion is the limiting factor that prevents the cluster D-TRILEX approach from restoring the translational invariance. These findings imply that a fully self-consistent algorithm, with the outer self-consistency loop that updates the reference system to preserve the equivalence between the inter- and intra-cluster self-energies, would lead to a complete restoration of the translational invariance within the cluster D-TRILEX scheme. However, performing such calculation will require recalculation of the two-particle quantities of the cluster impurity problem at every iteration of the outer-self-consistency loop, which is extremely expensive for the current implementation of the method.

IV. SUMMARY AND OUTLOOK

In this work we have developed and benchmarked a cluster extension of the D-TRILEX approach. We find that the method performs remarkably well for small-scale systems, such as a nano-ring Hubbard model. In particular, the cluster D-TRILEX improves the single-site version of the method and even outperforms much more computationally complex parquet D Γ A approach in predicting the self-energy at the most important points in momentum space, namely those lying at the Fermi energy. Far from the Fermi energy the D-TRILEX approach shows a non-causal behavior for the imaginary part of the self-energy in the case of small number of lattice sites, which can be cured by increasing the size of the system. Further, we have shown that the CDMFT reference problem is not well-suited to restore the translational invariance of the original lattice by perturbative diagrammatic extensions. To do so, it is necessary to perform a fully self-consistent solution of the problem by adjusting the cluster reference system.

Despite this limitation, the cluster extension of D-TRILEX offers an efficient framework for a combined treatment of

short- and long-range correlation effects. Its modest computational cost makes it a promising tool for exploring symmetry-broken states associated with not only local (e.g., charge density wave or spin ordered states) but also non-local (e.g., d -wave superconductivity) order parameters.

ACKNOWLEDGEMENTS

The authors acknowledge support from IDRIS/GENCI under grant number 091393, and are thankful to the CPHT computer support team for their help.

Appendix A: Rotation of the hybridization function

In this appendix we present the detained derivation of Eq. (8). Throughout the derivation we work with rotated dispersion $\bar{\varepsilon}_k$ and impurity self-energy $\bar{\Sigma}_v^{\text{imp}}$ defined as:

$$\bar{\varepsilon}_K = \mathcal{R} \varepsilon_K \mathcal{R}^\dagger \quad \text{and} \quad \bar{\Sigma}_v^{\text{imp}} = \mathcal{R} \Sigma_v^{\text{imp}} \mathcal{R}^\dagger. \quad (\text{A1})$$

For sake of simplicity, in what follows we will omit the superscript “imp” in the impurity self-energy. The expression for the rotated hybridization function can be found via the Dyson equation for the impurity Green’s function:

$$\bar{\Delta}_v = \mathbb{1}(i\nu + \mu) - \bar{\Sigma}_v - \left\{ \sum_K \left[\mathbb{1}(i\nu + \mu) - \bar{\varepsilon}_K - \bar{\Sigma}_v \right]^{-1} \right\}^{-1}. \quad (\text{A2})$$

In this expression, the term inside the curly brackets corresponds to the local part of the CDMFT Green’s function \hat{G}_{Kv} , which, according to the DMFT self-consistency condition is equal to the impurity Green’s function: $\sum_K \hat{G}_{Kv} = g_v^{\text{imp}}$. Let us perform the high-frequency expansion for the last term on the right-hand side:

$$\sum_K \left[\mathbb{1}(i\nu + \mu) - (\bar{\varepsilon}_K + \bar{\Sigma}_v) \right]^{-1} \simeq \frac{1}{i\nu + \mu} \left[\mathbb{1} + \sum_{n \geq 1} \sum_K \left(\frac{\bar{\varepsilon}_K + \bar{\Sigma}_v}{i\nu + \mu} \right)^n \right]. \quad (\text{A3})$$

The inverse of this expression reads:

$$\left[\mathbb{1} + \sum_{n \geq 1} \sum_K \left(\frac{\bar{\varepsilon}_K + \bar{\Sigma}_v}{i\nu + \mu} \right)^n \right]^{-1} = \sum_{m \geq 0} \left(- \sum_{n \geq 1} \sum_K \left(\frac{\bar{\varepsilon}_K + \bar{\Sigma}_v}{i\nu + \mu} \right)^n \right)^m. \quad (\text{A4})$$

We now disentangle the lowest-order pieces of the double series. Specifically, we single out the $m = 0$ slice, which produces the identity matrix $\mathbb{1}(i\nu + \mu)$, and the unique $m = 1$, $n = 1$ contribution, which yields the linear term $(i\nu + \mu) \sum_K (\bar{\varepsilon}_K + \bar{\Sigma}_v)/(i\nu + \mu) = \langle \bar{\varepsilon}_K \rangle + \bar{\Sigma}_v$. All other configurations are collected into the two residual sums: (i) $m = 1$ with $n \geq 2$, and (ii) $m \geq 2$ with any $n \geq 1$. Both start at the second order in the small parameter $(\bar{\varepsilon}_K + \bar{\Sigma}_v)/(i\nu + \mu)$ and

therefore constitute genuinely higher-order corrections:

$$\begin{aligned} & \left\{ \sum_K \left[\mathbb{1}(iv + \mu) - (\bar{\varepsilon}_K + \bar{\Sigma}_v) \right]^{-1} \right\}^{-1} = \\ & = \mathbb{1}(iv + \mu) - \langle \bar{\varepsilon}_K \rangle - \bar{\Sigma}_v - (iv + \mu) \sum_{n \geq 2} \sum_K \left(\frac{\bar{\varepsilon}_K + \bar{\Sigma}_v}{iv + \mu} \right)^n \\ & + (iv + \mu) \sum_{m \geq 2} \left(- \sum_{n \geq 1} \sum_K \left(\frac{\bar{\varepsilon}_K + \bar{\Sigma}_v}{iv + \mu} \right)^n \right)^m. \end{aligned} \quad (\text{A5})$$

We find, that the terms $\mathbb{1}(iv + \mu)$ and $\bar{\Sigma}_v$ cancel out with the corresponding terms in the definition of $\bar{\Delta}_v$ (A2). The final expression for the rotated hybridization becomes:

$$\begin{aligned} \bar{\Delta}(v) = & \langle \bar{\varepsilon}_K \rangle - (iv + \mu) \sum_{n \geq 2} \sum_K \left(\frac{\bar{\varepsilon}_K + \bar{\Sigma}_v}{iv + \mu} \right)^n \\ & + (iv + \mu) \sum_{m \geq 2} \left(- \sum_{n \geq 1} \sum_K \left(\frac{\bar{\varepsilon}_K + \bar{\Sigma}_v}{iv + \mu} \right)^n \right)^m. \end{aligned} \quad (\text{A6})$$

This relation implies that the most optimal basis that reduces off-diagonal components of the hybridization is the one that diagonalizes the local part of the electronic dispersion $\langle \bar{\varepsilon}_K \rangle$.

-
- [1] A. A. Abrikosov and I. M. Khalatnikov, The theory of a Fermi liquid (the properties of liquid 3He at low temperatures), *Rep. Prog. Phys.* **22**, 329 (1959).
 - [2] P. Nozières, *Theory Of Quantum Liquids* (CRC Press, 2018).
 - [3] L. Hedin, New Method for Calculating the One-Particle Green's Function with Application to the Electron-Gas Problem, *Phys. Rev.* **139**, A796 (1965).
 - [4] F. Aryasetiawan and O. Gunnarsson, The GW method, *Rep. Prog. Phys.* **61**, 237 (1998).
 - [5] L. Hedin, On correlation effects in electron spectroscopies and the GW approximation, *J. Phys. Condens. Matter* **11**, R489 (1999).
 - [6] N. E. Bickers and D. J. Scalapino, Conserving approximations for strongly fluctuating electron systems. I. Formalism and calculational approach, *Ann. Phys.* **193**, 206 (1989).
 - [7] N. E. Bickers, D. J. Scalapino, and S. R. White, Conserving Approximations for Strongly Correlated Electron Systems: Bethe-Salpeter Equation and Dynamics for the Two-Dimensional Hubbard Model, *Phys. Rev. Lett.* **62**, 961 (1989).
 - [8] A. I. Lichtenstein and M. I. Katsnelson, Ab initio calculations of quasiparticle band structure in correlated systems: LDA++ approach, *Phys. Rev. B* **57**, 6884 (1998).
 - [9] A. Georges, G. Kotliar, W. Krauth, and M. J. Rozenberg, Dynamical mean-field theory of strongly correlated fermion systems and the limit of infinite dimensions, *Rev. Mod. Phys.* **68**, 13 (1996).
 - [10] N. F. Mott, *Metal-insulator transitions* (London: Taylor & Francis, 1974).
 - [11] M. Imada, A. Fujimori, and Y. Tokura, Metal-insulator transitions, *Rev. Mod. Phys.* **70**, 1039 (1998).
 - [12] A. Georges, L. de Medici, and J. Mravlje, Strong Correlations from Hund's Coupling, *Annu. Rev. Condens. Matter Phys.* **4**, 137 (2013).
 - [13] A. Georges and G. Kotliar, The Hund-metal path to strong electronic correlations, *Physics Today* **77**, 46 (2024).
 - [14] W. Metzner and D. Vollhardt, Correlated Lattice Fermions in $d = \infty$ Dimensions, *Phys. Rev. Lett.* **62**, 324 (1989).
 - [15] E. Müller-Hartmann, Correlated Fermions on a Lattice in High Dimensions, *Z. Phys.* **74**, 507 (1989).
 - [16] M. Chatzieftheriou, S. Biermann, and E. A. Stepanov, Local and Nonlocal Electronic Correlations at the Metal-Insulator Transition in the Two-Dimensional Hubbard Model, *Phys. Rev. Lett.* **132**, 236504 (2024).
 - [17] M. Vandelli, J. Kaufmann, M. El-Nabulsi, V. Harkov, A. I. Lichtenstein, and E. A. Stepanov, Multi-band D-TRILEX approach to materials with strong electronic correlations, *SciPost Phys.* **13**, 036 (2022).
 - [18] A. Valli, T. Schäfer, P. Thunström, G. Rohringer, S. Andergassen, G. Sangiovanni, K. Held, and A. Toschi, Dynamical vertex approximation in its parquet implementation: Application to Hubbard nanorings, *Phys. Rev. B* **91**, 115115 (2015).
 - [19] M. H. Hettler, A. N. Tahvildar-Zadeh, M. Jarrell, T. Pruschke, and H. R. Krishnamurthy, Nonlocal dynamical correlations of strongly interacting electron systems, *Phys. Rev. B* **58**, R7475 (1998).
 - [20] A. I. Lichtenstein and M. I. Katsnelson, Antiferromagnetism and d-wave superconductivity in cuprates: A cluster dynamical mean-field theory, *Phys. Rev. B* **62**, R9283 (2000).
 - [21] G. Kotliar, S. Y. Savrasov, G. Pálsson, and G. Biroli, Cellular Dynamical Mean Field Approach to Strongly Correlated Systems, *Phys. Rev. Lett.* **87**, 186401 (2001).
 - [22] T. Maier, M. Jarrell, T. Pruschke, and M. H. Hettler, Quantum cluster theories, *Rev. Mod. Phys.* **77**, 1027 (2005).
 - [23] A.-M. S. Tremblay, B. Kyung, and D. Sénéchal, Pseudogap and high-temperature superconductivity from weak to strong coupling. Towards a quantitative theory (Review Article), *Low Temp. Phys.* **32**, 424 (2006).
 - [24] G. Kotliar, S. Y. Savrasov, K. Haule, V. S. Oudovenko, O. Parcollet, and C. A. Marianetti, Electronic structure calculations with dynamical mean-field theory, *Rev. Mod. Phys.* **78**, 865 (2006).
 - [25] H. Park, K. Haule, and G. Kotliar, Cluster Dynamical Mean Field Theory of the Mott Transition, *Phys. Rev. Lett.* **101**, 186403 (2008).
 - [26] K. Haule and G. Kotliar, Strongly correlated superconductivity: A plaquette dynamical mean-field theory study, *Phys. Rev. B* **76**, 104509 (2007).
 - [27] M. Civelli, M. Capone, A. Georges, K. Haule, O. Parcollet, T. D. Stanescu, and G. Kotliar, Nodal-Antinodal Dichotomy and the Two Gaps of a Superconducting Doped Mott Insulator, *Phys. Rev. Lett.* **100**, 046402 (2008).
 - [28] M. Harland, M. I. Katsnelson, and A. I. Lichtenstein, Plaquette valence bond theory of high-temperature superconductivity, *Phys. Rev. B* **94**, 125133 (2016).
 - [29] M. Harland, S. Brener, M. I. Katsnelson, and A. I. Lichtenstein, Exactly solvable model of strongly correlated d-wave superconductivity, *Phys. Rev. B* **101**, 045119 (2020).
 - [30] M. Danilov, E. G. C. P. van Loon, S. Brener, S. Isakov, M. I. Katsnelson, and A. I. Lichtenstein, Degenerate plaquette physics as key ingredient of high-temperature superconductivity in cuprates, *npj Quantum Mater.* **7**, 50 (2022).

- [31] X. Dong, E. Gull, and A. J. Millis, Quantifying the role of antiferromagnetic fluctuations in the superconductivity of the doped Hubbard model, *Nature Physics* **18**, 1293 (2022).
- [32] W. Wu, M. S. Scheurer, S. Chatterjee, S. Sachdev, A. Georges, and M. Ferrero, Pseudogap and Fermi-Surface Topology in the Two-Dimensional Hubbard Model, *Phys. Rev. X* **8**, 021048 (2018).
- [33] E. A. Stepanov, S. Isakov, M. I. Katsnelson, and A. I. Lichtenstein, *Superconductivity of Bad Fermions: Origin of Two Gaps in HTSC Cuprates*, Preprint arXiv:2502.08635 (2025).
- [34] J. E. Hirsch and R. M. Fye, Monte Carlo Method for Magnetic Impurities in Metals, *Phys. Rev. Lett.* **56**, 2521 (1986).
- [35] B. B. Beard and U.-J. Wiese, Simulations of Discrete Quantum Systems in Continuous Euclidean Time, *Phys. Rev. Lett.* **77**, 5130 (1996).
- [36] N. V. Prokof'ev, B. V. Svistunov, and I. S. Tupitsyn, Exact Quantum Monte Carlo Process for the Statistics of Discrete Systems, *JETP Letters* **64**, 911 (1996).
- [37] A. N. Rubtsov and A. I. Lichtenstein, Continuous-Time Quantum Monte Carlo Method for Fermions: Beyond Auxiliary Field Framework, *JETP Letters* **80**, 61 (2004).
- [38] A. N. Rubtsov, V. V. Savkin, and A. I. Lichtenstein, Continuous-time quantum Monte Carlo method for fermions, *Phys. Rev. B* **72**, 035122 (2005).
- [39] P. Werner, A. Comanac, L. de' Medici, M. Troyer, and A. J. Millis, Continuous-Time Solver for Quantum Impurity Models, *Phys. Rev. Lett.* **97**, 076405 (2006).
- [40] E. Gull, P. Werner, X. Wang, M. Troyer, and A. J. Millis, Local Order and the Gapped Phase of the Hubbard Model: A Plaquette Dynamical Mean-Field Investigation, *EPL* **84**, 37009 (2008).
- [41] E. Gull, A. J. Millis, A. I. Lichtenstein, A. N. Rubtsov, M. Troyer, and P. Werner, Continuous-time Monte Carlo methods for quantum impurity models, *Rev. Mod. Phys.* **83**, 349 (2011).
- [42] E. Y. Loh, J. E. Gubernatis, R. T. Scalettar, S. R. White, D. J. Scalapino, and R. L. Sugar, Sign problem in the numerical simulation of many-electron systems, *Phys. Rev. B* **41**, 9301 (1990).
- [43] E. Gorelov, T. O. Wehling, A. N. Rubtsov, M. I. Katsnelson, and A. I. Lichtenstein, Relevance of the complete Coulomb interaction matrix for the Kondo problem: Co impurities in Cu hosts, *Phys. Rev. B* **80**, 155132 (2009).
- [44] X. Wang and A. J. Millis, Quantum criticality and non-Fermi-liquid behavior in a two-level two-lead quantum dot, *Phys. Rev. B* **81**, 045106 (2010).
- [45] P. Werner and A. J. Millis, Hybridization expansion impurity solver: General formulation and application to Kondo lattice and two-orbital models, *Phys. Rev. B* **74**, 155107 (2006).
- [46] M. Civelli, M. Capone, S. S. Kancharla, O. Parcollet, and G. Kotliar, Dynamical Breakup of the Fermi Surface in a Doped Mott Insulator, *Phys. Rev. Lett.* **95**, 106402 (2005).
- [47] T. D. Stanescu and G. Kotliar, Fermi arcs and hidden zeros of the Green function in the pseudogap state, *Phys. Rev. B* **74**, 125110 (2006).
- [48] S. Sakai, G. Sangiovanni, M. Civelli, Y. Motome, K. Held, and M. Imada, Cluster-size dependence in cellular dynamical mean-field theory, *Phys. Rev. B* **85**, 035102 (2012).
- [49] A. A. Katanin, A. Toschi, and K. Held, Comparing pertinent effects of antiferromagnetic fluctuations in the two- and three-dimensional Hubbard model, *Phys. Rev. B* **80**, 075104 (2009).
- [50] G. Rohringer, H. Hafermann, A. Toschi, A. A. Katanin, A. E. Antipov, M. I. Katsnelson, A. I. Lichtenstein, A. N. Rubtsov, and K. Held, Diagrammatic routes to nonlocal correlations beyond dynamical mean field theory, *Rev. Mod. Phys.* **90**, 025003 (2018).
- [51] Y. S. Lyakhova, G. V. Astretsov, and A. N. Rubtsov, The mean-field concept and post-DMFT methods in the contemporary theory of correlated systems, *PHYS-USP+* **193**, 825–844 (2023), [*Phys. Usp.* 66 775–793 (2023)].
- [52] S. Isakov, A. E. Antipov, and E. Gull, Diagrammatic Monte Carlo for dual fermions, *Phys. Rev. B* **94**, 035102 (2016).
- [53] J. Gukelberger, E. Kozik, and H. Hafermann, Diagrammatic Monte Carlo approach for diagrammatic extensions of dynamical mean-field theory: Convergence analysis of the dual fermion technique, *Phys. Rev. B* **96**, 035152 (2017).
- [54] M. Vandelli, V. Harkov, E. A. Stepanov, J. Gukelberger, E. Kozik, A. Rubio, and A. I. Lichtenstein, Dual boson diagrammatic Monte Carlo approach applied to the extended Hubbard model, *Phys. Rev. B* **102**, 195109 (2020).
- [55] N. V. Prokof'ev and B. V. Svistunov, Polaron Problem by Diagrammatic Quantum Monte Carlo, *Phys. Rev. Lett.* **81**, 2514 (1998).
- [56] E. Kozik, K. Van Houcke, E. Gull, L. Pollet, N. Prokof'ev, B. Svistunov, and M. Troyer, Diagrammatic Monte Carlo for correlated fermions, *EPL* **90**, 10004 (2010).
- [57] S. Biermann, F. Aryasetiawan, and A. Georges, First-Principles Approach to the Electronic Structure of Strongly Correlated Systems: Combining the GW Approximation and Dynamical Mean-Field Theory, *Phys. Rev. Lett.* **90**, 086402 (2003).
- [58] P. Sun and G. Kotliar, Many-Body Approximation Scheme beyond GW, *Phys. Rev. Lett.* **92**, 196402 (2004).
- [59] T. Ayral, P. Werner, and S. Biermann, Spectral Properties of Correlated Materials: Local Vertex and Nonlocal Two-Particle Correlations from Combined GW and Dynamical Mean Field Theory, *Phys. Rev. Lett.* **109**, 226401 (2012).
- [60] T. Ayral, S. Biermann, and P. Werner, Screening and nonlocal correlations in the extended Hubbard model from self-consistent combined GW and dynamical mean field theory, *Phys. Rev. B* **87**, 125149 (2013).
- [61] L. Huang, T. Ayral, S. Biermann, and P. Werner, Extended dynamical mean-field study of the Hubbard model with long-range interactions, *Phys. Rev. B* **90**, 195114 (2014).
- [62] L. Boehnke, F. Nilsson, F. Aryasetiawan, and P. Werner, When strong correlations become weak: Consistent merging of GW and DMFT, *Phys. Rev. B* **94**, 201106 (2016).
- [63] T. Ayral, S. Biermann, P. Werner, and L. Boehnke, Influence of Fock exchange in combined many-body perturbation and dynamical mean field theory, *Phys. Rev. B* **95**, 245130 (2017).
- [64] N. Martin, C. Gauvin-Ndiaye, and A.-M. S. Tremblay, Nonlocal corrections to dynamical mean-field theory from the two-particle self-consistent method, *Phys. Rev. B* **107**, 075158 (2023).
- [65] K. Zantout, S. Backes, A. Razpopov, D. Lessnich, and R. Valentí, Improved effective vertices in the multiorbital two-particle self-consistent method from dynamical mean-field theory, *Phys. Rev. B* **107**, 235101 (2023).
- [66] O. Simard and P. Werner, Dynamical mean field theory extension to the nonequilibrium two-particle self-consistent approach, *Phys. Rev. B* **107**, 245137 (2023).
- [67] L. Geng, J. Yan, and P. Werner, Two-particle self-consistent approach combined with dynamical mean field theory: A real-frequency study of the square-lattice Hubbard model, *Phys. Rev. B* **111**, 115143 (2025).
- [68] J. B. Profe, J. Yan, K. Zantout, P. Werner, and R. Valentí, *Multi-orbital two-particle self-consistent approach – strengths and limitations*, Preprint arXiv:2410.00962 (2025).

- [69] A. N. Rubtsov, M. I. Katsnelson, and A. I. Lichtenstein, Dual fermion approach to nonlocal correlations in the Hubbard model, *Phys. Rev. B* **77**, 033101 (2008).
- [70] A. N. Rubtsov, M. I. Katsnelson, A. I. Lichtenstein, and A. Georges, Dual fermion approach to the two-dimensional Hubbard model: Antiferromagnetic fluctuations and Fermi arcs, *Phys. Rev. B* **79**, 045133 (2009).
- [71] H. Hafermann, G. Li, A. N. Rubtsov, M. I. Katsnelson, A. I. Lichtenstein, and H. Monien, Efficient Perturbation Theory for Quantum Lattice Models, *Phys. Rev. Lett.* **102**, 206401 (2009).
- [72] Brener, S. and Stepanov, Evgeny A. and Rubtsov, Alexey N. and Katsnelson, Mikhail I. and Lichtenstein, Alexander I., Dual fermion method as a prototype of generic reference-system approach for correlated fermions, *Ann. Phys.* **422**, 168310 (2020).
- [73] A. N. Rubtsov, M. I. Katsnelson, and A. I. Lichtenstein, Dual boson approach to collective excitations in correlated fermionic systems, *Ann. Phys.* **327**, 1320 (2012).
- [74] E. G. C. P. van Loon, A. I. Lichtenstein, M. I. Katsnelson, O. Parcollet, and H. Hafermann, Beyond extended dynamical mean-field theory: Dual boson approach to the two-dimensional extended Hubbard model, *Phys. Rev. B* **90**, 235135 (2014).
- [75] E. A. Stepanov, E. G. C. P. van Loon, A. A. Katanin, A. I. Lichtenstein, M. I. Katsnelson, and A. N. Rubtsov, Self-consistent dual boson approach to single-particle and collective excitations in correlated systems, *Phys. Rev. B* **93**, 045107 (2016).
- [76] E. A. Stepanov, A. Huber, E. G. C. P. van Loon, A. I. Lichtenstein, and M. I. Katsnelson, From local to nonlocal correlations: The Dual Boson perspective, *Phys. Rev. B* **94**, 205110 (2016).
- [77] E. A. Stepanov, L. Peters, I. S. Krivenko, A. I. Lichtenstein, M. I. Katsnelson, and A. N. Rubtsov, Quantum spin fluctuations and evolution of electronic structure in cuprates, *npj Quantum Mater.* **3**, 54 (2018).
- [78] L. Peters, E. G. C. P. van Loon, A. N. Rubtsov, A. I. Lichtenstein, M. I. Katsnelson, and E. A. Stepanov, Dual boson approach with instantaneous interaction, *Phys. Rev. B* **100**, 165128 (2019).
- [79] A. Toschi, A. A. Katanin, and K. Held, Dynamical vertex approximation: A step beyond dynamical mean-field theory, *Phys. Rev. B* **75**, 045118 (2007).
- [80] A. Galler, P. Thunström, P. Gunacker, J. M. Tomczak, and K. Held, Ab initio dynamical vertex approximation, *Phys. Rev. B* **95**, 115107 (2017).
- [81] A. Galler, J. Kaufmann, P. Gunacker, M. Pickem, P. Thunström, J. M. Tomczak, and K. Held, Towards ab initio Calculations with the Dynamical Vertex Approximation, *J. Phys. Soc. Jpn.* **87**, 041004 (2018).
- [82] J. Kaufmann, C. Eckhardt, M. Pickem, M. Kitatani, A. Kauch, and K. Held, Self-consistent ladder dynamical vertex approximation, *Phys. Rev. B* **103**, 035120 (2021).
- [83] T. Ayral and O. Parcollet, Mott physics and spin fluctuations: A unified framework, *Phys. Rev. B* **92**, 115109 (2015).
- [84] T. Ayral and O. Parcollet, Mott physics and spin fluctuations: A functional viewpoint, *Phys. Rev. B* **93**, 235124 (2016).
- [85] J. Vučković, T. Ayral, and O. Parcollet, TRILEX and GW+EDMFT approach to d -wave superconductivity in the Hubbard model, *Phys. Rev. B* **96**, 104504 (2017).
- [86] E. A. Stepanov, V. Harkov, and A. I. Lichtenstein, Consistent partial bosonization of the extended Hubbard model, *Phys. Rev. B* **100**, 205115 (2019).
- [87] V. Harkov, M. Vandelli, S. Brener, A. I. Lichtenstein, and E. A. Stepanov, Impact of partially bosonized collective fluctuations on electronic degrees of freedom, *Phys. Rev. B* **103**, 245123 (2021).
- [88] C. Lenihan, A. J. Kim, F. Šimkovic, and E. Kozik, Evaluating Second-Order Phase Transitions with Diagrammatic Monte Carlo: Néel Transition in the Doped Three-Dimensional Hubbard Model, *Phys. Rev. Lett.* **129**, 107202 (2022).
- [89] G. Rohringer and A. Toschi, Impact of nonlocal correlations over different energy scales: A dynamical vertex approximation study, *Phys. Rev. B* **94**, 125144 (2016).
- [90] T. Schäfer, N. Wentzell, F. Šimkovic, Y.-Y. He, C. Hille, M. Klett, C. J. Eckhardt, B. Arzhang, V. Harkov, F.-M. Le Régent, A. Kirsch, Y. Wang, A. J. Kim, E. Kozik, E. A. Stepanov, A. Kauch, S. Andergassen, P. Hansmann, D. Rohe, Y. M. Vilk, J. P. F. LeBlanc, S. Zhang, A.-M. S. Tremblay, M. Ferrero, O. Parcollet, and A. Georges, Tracking the Footprints of Spin Fluctuations: A MultiMethod, MultiMessenger Study of the Two-Dimensional Hubbard Model, *Phys. Rev. X* **11**, 011058 (2021).
- [91] M. Vandelli, *Quantum embedding methods in dual space for strongly interacting electronic systems*, Ph.D. thesis, Universität Hamburg Hamburg (2022).
- [92] T. Schäfer, F. Geles, D. Rost, G. Rohringer, E. Arrigoni, K. Held, N. Blümer, M. Aichhorn, and A. Toschi, Fate of the false Mott-Hubbard transition in two dimensions, *Phys. Rev. B* **91**, 125109 (2015).
- [93] F. Šimkovic, J. P. F. LeBlanc, A. J. Kim, Y. Deng, N. V. Prokof'ev, B. V. Svistunov, and E. Kozik, Extended Crossover from a Fermi Liquid to a Quasiantiferromagnet in the Half-Filled 2D Hubbard Model, *Phys. Rev. Lett.* **124**, 017003 (2020).
- [94] A. J. Kim, F. Šimkovic, and E. Kozik, Spin and Charge Correlations across the Metal-to-Insulator Crossover in the Half-Filled 2D Hubbard Model, *Phys. Rev. Lett.* **124**, 117602 (2020).
- [95] IV, Fedor Šimkovic and Rossi, Riccardo and Ferrero, Michel, Two-dimensional Hubbard model at finite temperature: Weak, strong, and long correlation regimes, *Phys. Rev. Res.* **4**, 043201 (2022).
- [96] J. Otsuki, H. Hafermann, and A. I. Lichtenstein, Superconductivity, antiferromagnetism, and phase separation in the two-dimensional Hubbard model: A dual-fermion approach, *Phys. Rev. B* **90**, 235132 (2014).
- [97] M. Kitatani, N. Tsuji, and H. Aoki, FLEX+DMFT approach to the d -wave superconducting phase diagram of the two-dimensional Hubbard model, *Phys. Rev. B* **92**, 085104 (2015).
- [98] M. Kitatani, T. Schäfer, H. Aoki, and K. Held, Why the critical temperature of high- T_c cuprate superconductors is so low: The importance of the dynamical vertex structure, *Phys. Rev. B* **99**, 041115 (2019).
- [99] M. Kitatani, L. Si, O. Janson, R. Arita, Z. Zhong, and K. Held, Nickelate superconductors — a renaissance of the one-band Hubbard model, *npj Quantum Mater.* **5**, 59 (2020).
- [100] T. Maier, M. Jarrell, T. Pruschke, and J. Keller, d -Wave Superconductivity in the Hubbard Model, *Phys. Rev. Lett.* **85**, 1524 (2000).
- [101] E. Gull, O. Parcollet, and A. J. Millis, Superconductivity and the Pseudogap in the Two-Dimensional Hubbard Model, *Phys. Rev. Lett.* **110**, 216405 (2013).
- [102] E. Kamil, J. Berges, G. Schönhoff, M. Rösner, M. Schüler, G. Sangiovanni, and T. Wehling, Electronic structure of single layer 1T-NbSe₂: interplay of lattice distortions, non-local exchange, and Mott-Hubbard correlations, *J. Phys. Condens.*

- Matter **30** (2018).
- [103] E. A. Stepanov, V. Harkov, M. Rösner, A. I. Lichtenstein, M. I. Katsnelson, and A. N. Rudenko, Coexisting charge density wave and ferromagnetic instabilities in monolayer InSe, *npj Comput. Mater.* **8**, 118 (2022).
 - [104] E. A. Stepanov, M. Vandelli, A. I. Lichtenstein, and F. Lechermann, Charge Density Wave Ordering in NdNiO₂: Effects of Multiorbital Nonlocal Correlations, *npj Comput. Mater.* **10**, 108 (2024).
 - [105] Y. M. Vilk and A.-M. S. Tremblay, Destruction of Fermi-liquid Quasiparticles in Two Dimensions by Critical Fluctuations, *EPL* **33**, 159 (1996).
 - [106] E. G. C. P. van Loon, H. Hafermann, A. I. Lichtenstein, A. N. Rubtsov, and M. I. Katsnelson, Plasmons in Strongly Correlated Systems: Spectral Weight Transfer and Renormalized Dispersion, *Phys. Rev. Lett.* **113**, 246407 (2014).
 - [107] L. Boehnke, P. Werner, and F. Lechermann, Multi-orbital nature of the spin fluctuations in Sr₂RuO₄, *EPL* **122**, 57001 (2018).
 - [108] S. Acharya, D. Pashov, C. Weber, H. Park, L. Sponza, and M. V. Schilfgaarde, Evening out the spin and charge parity to increase T_c in Sr₂RuO₄, *Commun. Phys.* **2**, 163 (2019).
 - [109] H. Suzuki, L. Wang, J. Bertinshaw, H. U. R. Strand, S. Käser, M. Krautloher, Z. Yang, N. Wentzell, O. Parcollet, F. Jerzembek, N. Kikugawa, A. P. Mackenzie, A. Georges, P. Hansmann, H. Gretarsson, and B. Keimer, Distinct spin and orbital dynamics in Sr₂RuO₄, *Nature Commun.* **14**, 7042 (2023).
 - [110] M. Vandelli, A. Galler, A. Rubio, A. I. Lichtenstein, S. Biermann, and E. A. Stepanov, Doping-dependent Charge- and Spin-Density Wave Orderings in a Monolayer of Pb Adatoms on Si(111), *npj Quantum Mater.* **9**, 19 (2024).
 - [111] E. A. Stepanov, M. Chatzieftheriou, N. Wagner, and G. Sangiovanni, Interconnected renormalization of Hubbard bands and Green's function zeros in Mott insulators induced by strong magnetic fluctuations, *Phys. Rev. B* **110**, L161106 (2024).
 - [112] E. A. Stepanov, Signatures of a Charge Ice State in the Doped Mott Insulator Nb₃Cl₈, Preprint arXiv:2405.19114 (2024).
 - [113] E. A. Stepanov, Y. Nomura, A. I. Lichtenstein, and S. Biermann, Orbital Isotropy of Magnetic Fluctuations in Correlated Electron Materials Induced by Hund's Exchange Coupling, *Phys. Rev. Lett.* **127**, 207205 (2021).
 - [114] E. A. Stepanov, Eliminating Orbital Selectivity from the Metal-Insulator Transition by Strong Magnetic Fluctuations, *Phys. Rev. Lett.* **129**, 096404 (2022).
 - [115] M. Vandelli, J. Kaufmann, V. Harkov, A. I. Lichtenstein, K. Held, and E. A. Stepanov, Extended regime of metastable metallic and insulating phases in a two-orbital electronic system, *Phys. Rev. Res.* **5**, L022016 (2023).
 - [116] E. A. Stepanov and S. Biermann, Can Orbital-Selective Néel Transitions Survive Strong Nonlocal Electronic Correlations?, *Phys. Rev. Lett.* **132**, 226501 (2024).
 - [117] M. Chatzieftheriou, A. N. Rudenko, Y. Sidis, S. Biermann, and E. A. Stepanov, Orbital-Selective Diffuse Magnetic Fluctuations in Sr₂RuO₄: a Unified Theoretical Picture, Preprint arXiv:2412.14735 (2025).
 - [118] N. Dasari, H. U. R. Strand, M. Eckstein, A. I. Lichtenstein, and E. A. Stepanov, Electron-magnon dynamics triggered by an ultrashort laser pulse: A real-time dual gw study, *Phys. Rev. B* **111**, 235129 (2025).
 - [119] H. Hafermann, S. Brener, A. N. Rubtsov, M. I. Katsnelson, and A. I. Lichtenstein, Cluster Dual Fermion Approach to Nonlocal Correlations, *JETP Letters* **86**, 677 (2008).
 - [120] S.-X. Yang, H. Fotso, H. Hafermann, K.-M. Tam, J. Moreno, T. Pruschke, and M. Jarrell, Dual fermion dynamical cluster approach for strongly correlated systems, *Phys. Rev. B* **84**, 155106 (2011).
 - [121] S. Isakov, H. Terletska, and E. Gull, Momentum-space cluster dual-fermion method, *Phys. Rev. B* **97**, 125114 (2018).
 - [122] S. Isakov, M. I. Katsnelson, and A. I. Lichtenstein, Perturbative solution of fermionic sign problem in quantum Monte Carlo computations, *npj Comput. Mater.* **10**, 36 (2024).
 - [123] T. Ayral, J. Vučković, and O. Parcollet, Fierz Convergence Criterion: A Controlled Approach to Strongly Interacting Systems with Small Embedded Clusters, *Phys. Rev. Lett.* **119**, 166401 (2017).
 - [124] P. Sémon and A.-M. S. Tremblay, Importance of subleading corrections for the Mott critical point, *Phys. Rev. B* **85**, 201101 (2012).
 - [125] H. Shinaoka, Y. Nomura, S. Biermann, M. Troyer, and P. Werner, Negative sign problem in continuous-time quantum Monte Carlo: Optimal choice of single-particle basis for impurity problems, *Phys. Rev. B* **92**, 195126 (2015).
 - [126] G. Biroli, O. Parcollet, and G. Kotliar, Cluster dynamical mean-field theories: Causality and classical limit, *Phys. Rev. B* **69**, 205108 (2004).
 - [127] J. Kanamori, Electron Correlation and Ferromagnetism of Transition Metals, *Prog. Theor. Phys.* **30**, 275 (1963).
 - [128] M. Wallerberger, A. Hausoel, P. Gunacker, A. Kowalski, N. Parragh, F. Goth, K. Held, and G. Sangiovanni, w2dynamics: Local one- and two-particle quantities from dynamical mean field theory, *Comput. Phys. Commun.* **235**, 388 (2019).